Binary Cellulose Nanocrystal Blends for Bioinspired Damage Tolerant Photonic Films

Bharath Natarajan, Ajay Krishnamurthy, Xin Qin, Caglar D. Emiroglu, Amanda Forster, E. Johan Foster, Christoph Weder, Douglas M. Fox, Sinan Keten, Jan Obrzut, and Jeffrey W. Gilman*

Most attempts to emulate the mechanical properties of strong and tough natural composites using helicoidal films of wood-derived cellulose nanocrystals (w-CNCs) fall short in mechanical performance due to the limited shear transfer ability between the w-CNCs. This shortcoming is ascribed to the small w-CNC-w-CNC overlap lengths that lower the shear transfer efficiency. Herein, we present a simple strategy to fabricate superior helicoidal CNC films with mechanical properties that rival those of the best natural materials and are some of the best reported for photonic CNC materials thus far. Assembling the short w-CNCs with a minority fraction of high aspect ratio CNCs derived from tunicates (t-CNCs), we report remarkable simultaneous enhancement of all in-plane mechanical properties and out-of-plane flexibility. The important role of t-CNCs is revealed by coarse grained molecular dynamics simulations where the property enhancement are due to increased interaction lengths and the activation of additional toughening mechanisms. At t-CNC contents greater than 5% by mass the mixed films also display UV reflecting behaviour. These damage tolerant optically active materials hold great promise for application as protective coatings. More broadly, we expect the strategy of using length-bidispersity to be adaptable to mechanically enhancing other matrix-free nanoparticle ensembles.

1. Introduction

Biological systems, through evolution, have developed mechanically resilient composites by using a combination of intricate hierarchical structural paradigms and constituent selection.[1–3] These materials are often multifunctional, combining desirable structural attributes like high fracture toughness, high elastic modulus, tolerance to impact, resistance to fatigue, stability in extreme environments, and self-healing behavior.[1–3] The evolutionarily convergent solution to achieve such functionality appears to be the use of nanocomposite architectures that are comprised of a majority fraction of a long-range ordered hard phase that is interspersed periodically with a soft macromolecular binder. While in a few select materials such as nacre the arrangement resembles stacked brick and mortar,[4] in the majority of biological composites (e.g., mantis shrimp dactyl club,[5] bone,[4,6] crustacean shells,[7] turtle carapace,[8] and ivory[9]) the microstructural motif is a helicoidal structure. Here, the constituents, typically in fibrillar form, are arranged in layers stacked in a helical fashion (**Figure 1**a).[10]

Biological helicoidal composites have the unique quality of being tough without being excessively ductile. Their toughness is attributed to structural or extrinsic toughening mechanisms at fixed length scales, which arise from the hierarchical and periodic arrangement of the hard and soft phases. These mechanisms, which include crack bridging, deflection, arrest and twisting, help maximize energy dissipation.[11] While crack bridging provides toughening by halting further crack opening and minimizing crack-tip stress concentration, crack deflection slows crack propagation by increasing

Dr. B. Natarajan, Dr. A. Krishnamurthy, Dr. C. D. Emiroglu, Dr. A. Forster, Dr. J. Obrzut, Dr. J. W. Gilman
Material Measurement Laboratory
National Institute of Standards and Technology
Gaithersburg, MD 20899, USA
E-mail: jeffrey.gilman@nist.gov

Dr. B. Natarajan, Dr. C. D. Emiroglu
Department of Physics
Georgetown University
Washington, DC 20057, USA

Dr. A. Krishnamurthy
Theiss Research
La Jolla, CA 92037, USA

X. Qin, Prof. S. Keten
Department of Mechanical Engineering
Northwestern University
Evanston, IL 60208, USA

Prof. E. J. Foster
Materials Science and Engineering
Virginia Tech Blacksburg
VA 24061, USA

Prof. C. Weder
Adolphe Merkle Institute
University of Fribourg
CH-1700 Fribourg, Switzerland

Prof. D. M. Fox
Department of Chemistry
American University
Washington, DC 20016, USA
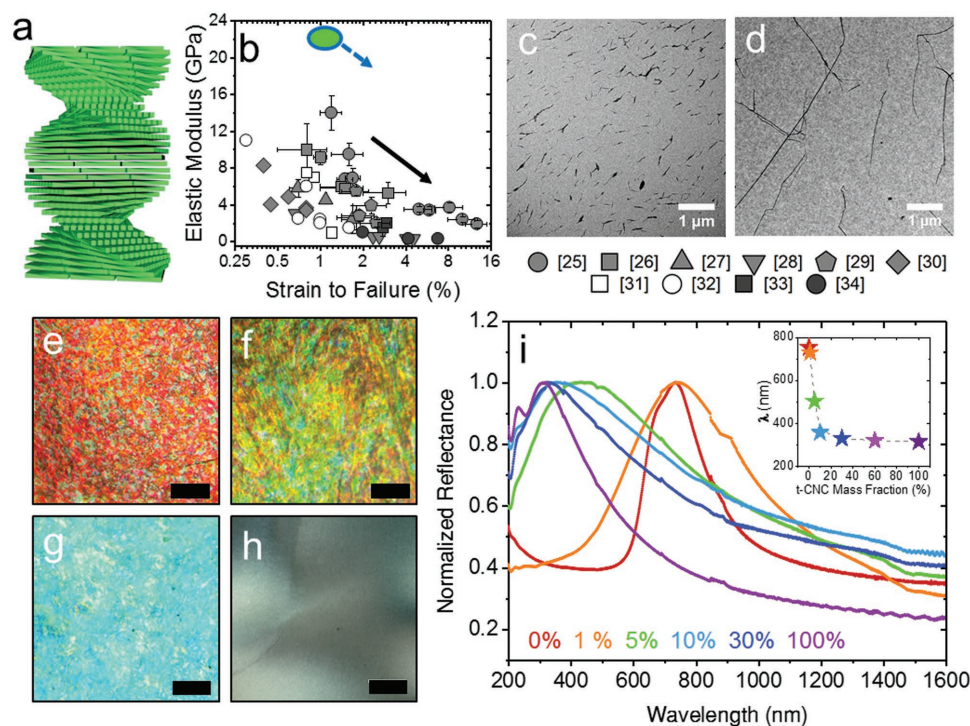
Figure 1. a) Schematic of model helicoidal structure formed by the assembly of cellulose nanocrystals. b) Comparative Ashby plot of the elastic modulus (GPa) versus the strain to failure (%) from helicoidal CNC films and composites reported in literature.[25–34] Error bars represent reported uncertainties. The black arrow represents the general trend in property change with increased polymer addition. The legend for panel (b) is presented below images (c) and (d). Transmission electron microscopy images of c) wood- and d) tunicate-derived CNCs. Polarized optical microscopy images of mixed w-CNC/t-CNC films containing e) 0%, f) 1%, g) 5%, and h) 100% by mass t-CNCs obtained in reflection mode. Scale bars are 0.5 mm. i) Plot of representative normalized (arbitrary units) reflectance versus wavelength (nm) for the various films (spectrum from 60% t-CNC film not shown for clarity). The inset shows plot of peak reflectance wavelength versus t-CNC mass fraction.

crack tortuosity. Crack twisting by the helical arrangement decelerates strain energy release at the crack tip and allows multiple cracks to grow from various nucleation sites without coalescing. The high crack surface to volume ratio maximizes energy dissipation.[1,3,6,11] In addition, recent studies have found the periodic helicoidal structure to exhibit phononic bandgaps that cause shear wave filtering and lead to enhanced impact tolerance.[12]

These extraordinary characteristics of "mechanofunctional" biological materials have motivated numerous efforts to fabricate and/or engineer nanocomposites that emulate their underlying structural design.[2] The "brick-and-mortar" architecture of nacre has been mimicked with a great degree of success using both top-down (3D printing[13] and layer-by-layer assembly)[2] as well as bottom-up assembly[14] (ice templating,[15] crystallization[16]) of nanomaterials like alumina and graphene platelets. While top-down methods such as 3D printing and carbon fibre layup have been employed to understand the advantages offered by the helicoidal stacking in microcomposites,[11,17] there have been few successful attempts at replicating the helicoidal structure using nano-sized components.[13] This may be directly attributable to the increased complexity of adding a periodic twist to the layer-by-layer stacking of the filler phase. That said, cellulose nanocrystals (CNCs) are rod-like particles that readily self-assemble into helicoidal (or chiral nematic or cholesteric) structures in aqueous suspensions.[18] This liquid

crystalline behavior is attributed to the screw-like twisting of the CNCs along their long axis.[19] The CNC suspensions, when dried appropriately, produce vitrified CNC films with the underlying helicoidal structure retained, but with periodicities in the visible wavelength range, resulting in brilliant structural coloration.[18]

The CNCs are typically isolated by the controlled acid hydrolysis of sustainable cellulosic biomass such as wood, cotton, bacteria, and tunicates. They vary greatly in size, shape, and crystallinity, mainly depending on the source material but also the specific isolation process.[20–23] For example, wood-derived CNCs (w-CNC) have square cross-sections (6 nm to 8 nm × 6 nm to 8 nm), low aspect ratios (AR ≈ 20, length ≈110 nm) and crystallinities of ≈60%. In contrast, CNCs isolated from tunicates (t-CNCs), sessile sea creatures, are longer (AR ≈ 100, length ≈1000 nm), more crystalline (≈ 80%) and display larger, rectangular cross-sections (6 nm to 9 nm × 12 nm to 20 nm). Owing to the high degree of crystallinity, CNCs exhibit outstanding mechanical properties that rival commercial materials such as stainless steel and Kevlar. These characteristics identify CNCs as excellent candidate building blocks for helicoidal nanocomposites. However, efforts to emulate helicoidal bio-nanomaterials with CNCs have been met with limited success.[24] The best of these biomimetic materials fall well short of the properties of the gold-standard biological materials such as cortical bone, ivory, and the mantis shrimp dactyl club

(Figure S3a, Supporting Information). This gap is attributable to the following observations. All studies on cellulose-rich helicoidal materials utilize w-CNCs as building blocks[25–34] and the mechanical properties of the pristine w-CNC films (100% w-CNC) leave much to be desired. The pristine w-CNC films are excessively brittle (strain to failure <0.5%). Several reports discuss the difficulty in characterizing the in-plane properties of the pristine w-CNC films due to their brittle nature.[25,30] While the materials' ductility may be improved with polymer/plasticizer addition, the enhancement comes at the cost of the elastic modulus (Figure 1b; Figure S3b, Supporting Information). From this inverse relationship between the modulus and ductility, we infer that the modulus of the pristine CNC film places the limit for the highest modulus achievable by composite formation with a polymer. As the modulus of the pure helicoidal w-CNC films do not exceed ≈10 GPa, the properties of w-CNC nanocomposites remain unremarkable, specifically when taking other biomaterials as the reference (Figure 1b; Figure S3, Supporting Information).[24,27,31] In order to successfully implement the polymer nanocomposites approach to mimick tough biological materials using CNCs, we need pristine CNC films to be significantly stiffer and more ductile (green region in Figure 1b). Using this approach, even with polymer addition, the final mechanical properties are likely to be comparable to the properties of the best biological materials.

The modulus and strength of individual w-CNC rods have been measured to be as high as 100 to 150 GPa (transverse-axial)[35,36] and 3 GPa,[37] respectively. However, the properties of helicoidal w-CNC films are over an order of magnitude lower. This mismatch in performance between individual nanorods and their ensembles is because ensemble properties are strongly influenced by the strength and density of their weakest elements.[38] Here, these elements correspond to weak CNC–CNC interfaces, short interaction lengths in low aspect ratio w-CNCs, and heterogeneities such as grain boundaries and voids that lead to strain localization.[39] In this article, we report a facile strategy for the fabrication of biomimetic pristine CNC films with superior stiffness, ductility, and toughness. This involves assembling wood CNCs with a minority fraction of high aspect ratio tunicate CNCs that serve to improve the shear transfer capability of CNC–CNC interfaces.

By varying the mass fraction of t-CNCs, we have been able to tune the photonic properties of the CNC films over the entire optical spectrum and further into the near ultraviolet (UV) range (736 nm ± 5 nm to 314 nm ± 3 nm). More importantly, by adding t-CNCs remarkable simultaneous improvements in the in-plane modulus, tensile strength, strain to failure, toughness, and out-of-plane ductility could be achieved. These results are rare for synthetic systems, which are characteristically limited by trade-offs. The properties measured here, while rivalling those of the gold-standard natural materials like bone and nacre, are also the highest reported thus far for the pristine chiral nematic CNC films.[25–34] The enhancements achieved upon introducing a minor fraction of t-CNCs are attributed to a) an increased overlap length that enhances shear transfer and presents bigger integrated energetic barriers to deformation through stronger nonbonded interactions and b) superior contribution of t-CNCs to structural toughening through crack

deflection and bridging. We note that t-CNCs were used as a testbed and that other, more technologically viable, sources for high-aspect ratio CNCs exist, including for example waste from banana farming operations.[40] The design concept presented here appears to be an excellent starting point for the development of tough, naturally sourced, UV-reflecting materials that are potentially useful as protective coatings in the automobile, aerospace, and infrastructure industries.
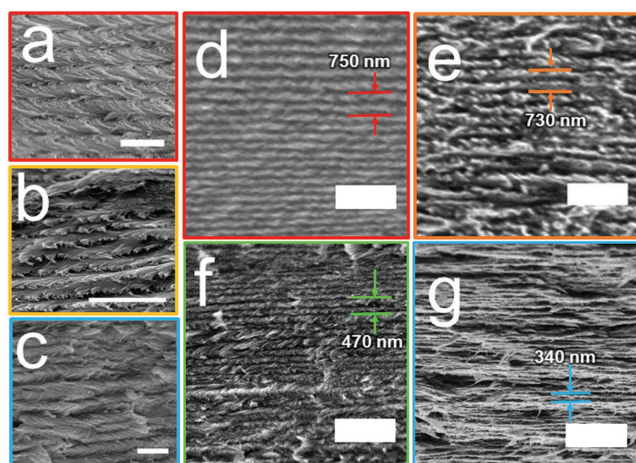
2. Results and Discussion

The dimensions of the wood and tunicate CNCs, used herein were obtained by analysis of transmission electron microscopy (TEM) images (Figure 1c,d; Figure S1a–d, Supporting Information). The w-CNCs had an average diameter (d), length (l), and aspect ratio (AR) of 7.8 nm ± 1.3 nm, 110.4 nm ± 36.7 nm, 14.2 ± 4.7, respectively (uncertainties represent one standard deviation in measured values). The t-CNCs were expectedly longer and wider with d, l, and AR measuring 13.1 nm ± 3.4 nm, 1228 nm ± 755.5 nm, 93.8 ± 57, respectively. The mixed w-CNC/t-CNC helicoidal films with varying fractions of t-CNCs (0%, 1%, 5%, 10%, 30%, 60% and 100% by mass) and w-CNCs were prepared by the evaporation induced self-assembly (EISA) of aqueous CNC mixtures in a custom-built chamber, which enabled controlled drying at desired evaporation rates (see the Experimental Section and Figure S2, Supporting Information). The evaporation rate was fixed at −7 mg min^{-1}, which we have found to yield films with good large-scale homogeneity. We note that it is essential to maintain the same drying rate over all samples, as minor variations in drying profiles result in major structural differences.[41]

Polarized optical microscope (POM) images of the mixed films, obtained in reflection mode, display a prominent blue shifting of structural color, which increased with the t-CNC content (Figure 1e–g). The films were observed to transition from red to orange-green to blue to colorless in going from 0 to 10% CNC. The films remained colorless at higher weight fractions (Figure 1h). UV–vis spectra of the dried films revealed a continuous nonlinear reduction in peak reflectance wavelength (λ) from red to ultraviolet (<400 nm) values with increased t-CNC concentration (Figure 1i and inset). Upon increasing the t-CNC content from 0 to 10% to 100% by mass, the λ decreased from 736 nm ± 5 nm to 357 nm ± 17 nm and asymptoted to the pristine t-CNC film wavelength of 314 nm ± 3 nm. These λ values are in qualitative agreement with the structural colors seen in the POM images (Figure 1e–h). Evidently, the high content (≥10% by mass) t-CNC films are colorless as they reflect in the UV range. In addition to the change of the reflectance wavelength, a broadening of the reflectance peak is observed (Figure 1i; Table S1, Supporting Information), which is indicative of an initial reduction in the film uniformity.[41] This is likely due to the increased polydispersity in CNC dimensions with the introduction of t-CNCs. However, increasing the mass fraction toward a majority t-CNC phase (≥30% t-CNC by mass) results in a restoration of uniformity.

Bouligand curves, characteristic of chiral nematic self-assembly, are observed in scanning electron microscopy (SEM) images of the film cross-sections, thereby confirming the

**ADVANCED
SCIENCE NEWS**

www.advancedsciencenews.com

**ADVANCED
FUNCTIONAL
MATERIALS**

www.afm-journal.de

Figure 2. High-magnification SEM images of the cross sections of the mixed w-CNC/t-CNC films with a) 0%, b) 1%, and c) 10% by mass t-CNCs, showing Bouligand patterns characteristic of helicoidal assembly. The scale bars represent 1 μm. d–g) SEM images of the cross sections of the mixed films containing d) 0%, e) 1%, f) 5%, and g) 10% by mass t-CNCs, showing periodic patterns representative of chiral nematic architecture and corresponding pitch measurements. The scale bars represent 2 μm.

helicoidal architecture of the mixed films (**Figure 2**a–c). It is interesting to note that the t-CNCs are also arranged in a helicoidal pattern in their native organism.[42] The mean pitch (P), computed from SEM images, was found to correlate with λ, in accordance with the relation $\lambda = (nP/2)$,[43] where n is the refractive index (≈ 2[41]), confirming that the microstructural evolution with t-CNC addition is indeed responsible for the observed trends in optical response (Figure 2d–g; Figure S4 and associated text, Supporting Information). It was not possible to reliably quantify the cross-sectional features in the 30%, 60%, and 100% t-CNC films, owing to surface roughness and protruding long t-CNCs that obscure the underlying periodic structure. We discuss this observation later in relation to the materials' mechanical properties. We note that in all samples the t-CNCs are fairly well integrated with the w-CNCs (Figure S9, Supporting Information), indicating excellent compatibility between the two different CNC types. That is, a large-scale phase separation, which would cause SEM cross-sections to exhibit distinct domains of layered w-CNCs and pulled out t-CNCs, was not observed. While these two CNC types,

individually, have been extensively used to create polymer nanocomposites and neat CNC films, polymer-free mixtures containing both these CNC types (or other mixtures of CNC with dissimilar aspect ratios) have so far not been reported. Further, we note that while helicoidal films of w-CNCs have been widely studied, those of longer CNCs have thus far not been reported.

Our results suggest that the t-CNCs lead to lower pitch and larger angular shifts between the helicoidally stacked w-CNC layers (Table S1, Supporting Information). The observed effects may be because t-CNCs nucleate and/or template w-CNC assembly, as they are larger in size and crystallinity and/or modify the ionic strength of solutions acting as solid electrolytes.[44] Further, from inductively coupled plasma mass spectrometry we observe a slightly higher concentration of multivalent metal ions in the t-CNC solutions (Table S2, Supporting Information). While this small concentration is unlikely to directly influence CNC–CNC interactions in the film, the slightly increased ionic strength in the t-CNC solutions may also cause a lowering of the pitch.[45] The exact role of t-CNCs in the self-assembly process remains to be explored. We believe that the detailed in situ characterization of the blends as they dry using techniques such as super-resolution optical microscopy (structured illumination microscopy in particular) and small angle X-ray or neutron scattering hold the key to understand the influence of the t-CNCs. Regardless, our findings indicate the ability to the tune the photonic properties of the CNC films from the infrared to the ultraviolet range by the addition of tunicate CNCs.

The uniaxial mechanical properties of the blended chiral films, measured by tensile testing under controlled strain rate (0.09 mm min^{-1}), are summarized in **Table 1** and **Figure 3**. The properties of the pure w-CNC films are in general agreement with the measurements reported by other researchers.[25,26,29,30] The 100% w-CNC films are extremely brittle (strain to failure $\approx 0.36\% \pm 0.1\%$) and difficult to handle. Further their elastic modulus (E) is measured to be 9.1 ± 0.5 GPa which is at the high-end of moduli measured for the chiral-CNC composites (Figure 1b).[27,31] Nevertheless, with the introduction of t-CNCs extraordinary enhancements in modulus (E), strain-to-failure (ε_f), tensile strength (σ_f), and toughness are observed (Figure 3a–d). This remarkable behavior is highlighted in Figure 3e, where stress–strain curves pan upward and outward with the increasing t-CNC concentration. The inclusion of up to 30% t-CNCs, results in sharp improvements, by factors of 2 and

Table 1. Modulus (GPa), tensile strength (MPa), strain to failure (%), toughness (MJ m^{-3}), and peak reflectance wavelength (nm) values of mixed w-CNC/t-CNC films containing 0%–100% t-CNCs by mass. Uncertainties represent one standard deviation in measured values from at least five samples.

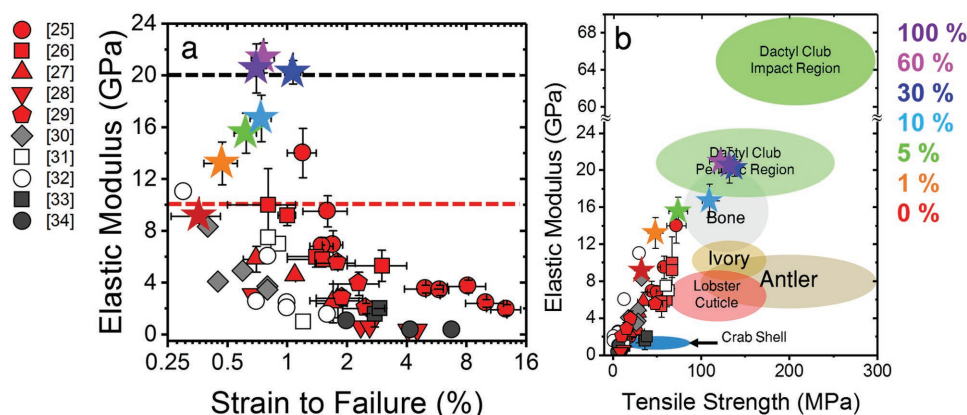| Mass fraction t-CNC [%]	Modulus, E [GPa]	Tensile strength, σ_f [MPa]	Strain to failure, ε_f [%]	Toughness [MPa m^{-3}]	Peak reflectance wavelength [nm]
0	9.1 ± 0.5	32.9 ± 5.0	0.36 ± 0.10	0.06 ± 0.02	736 ± 5
1	13.2 ± 1.7	48.42 ± 5.8	0.47 ± 0.09	0.11 ± 0.01	729 ± 3
5	15.5 ± 1.6	74.2 ± 10.6	0.62 ± 0.08	0.23 ± 0.02	502 ± 9
10	16.7 ± 1.8	109.7 ± 8.5	0.74 ± 0.09	0.44 ± 0.01	357 ± 17
30	20.2 ± 0.9	138 ± 4.3	1.07 ± 0.10	1.01 ± 0.01	329 ± 3
60	21.4 ± 1.2	122.3 ± 12.6	0.76 ± 0.10	0.56 ± 0.01	319 ± 3
100	20.5 ± 1.9	132.3 ± 10	0.70 ± 0.05	0.46 ± 0.01	314 ± 3
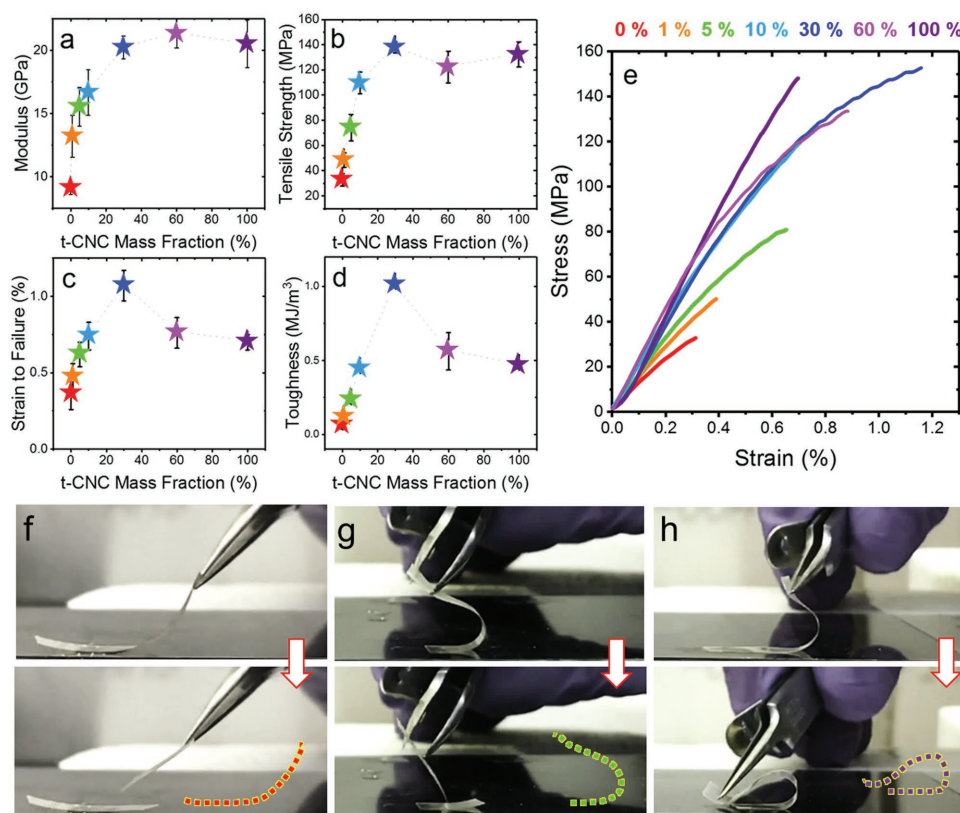
Figure 3. Plots of a) modulus (GPa), b) tensile strength (MPa), c) strain to failure (%), and d) toughness (MJ m^{-3}) of mixed w-CNC/t-CNC films versus t-CNC mass fraction (%). Error bars represent one standard deviation in measured values for at least five samples. e) Representative stress–strain curves measured by in-plane tensile testing of the various CNC films, with concentration of t-CNC indicated in the legend. Snapshots from videos of out-of-plane ductility tests from mixed w-CNC/t-CNC films containing f) 0%, g) 5%, and h) 30% by mass t-CNCs. The dashed profiles represent final shape before failure. Note that the 30% t-CNC sample in panel (h) does not fail in these tests.

4.5, in E and σ_f, over the corresponding properties of the 100% w-CNC films (Figure 3a,b and Table 1). With further t-CNC addition, E and σ_f plateau (within error) to the 60% and 100% t-CNC film values of ≈20.5 GPa and ≈130 MPa, respectively. In contrast, ε_f is observed to reach a maximum of 1.1% (≈3.5 × $\varepsilon_{f, 100\% \text{ w-CNC}}$) at 30% t-CNC by mass, before dropping to 0.76% and 0.70% for the 60% and 100% t-CNC films (**Figure 4**c and Table 1), respectively. The improvements in E, ε_f, and σ_f manifest as exceptional enhancements in toughness (measured as the area under stress–strain curve), which, following ε_f, peaks at 30% by mass t-CNC. Specifically, 8-fold and 19-fold toughness enhancements are observed in 10% and 30% by mass t-CNC films, respectively (Figure 3c and Table 1). These mass fractions translate to number fractions as small as 0.3% and 1.3%, respectively. Such enhancement at low t-CNC addition is of great practical significance, since acquisition and processing costs of t-CNC (and other high-aspect ratio CNCs) tunicates remain high when compared to w-CNCs. It is interesting to note that Weder and co-workers have similar observations regarding strong influence of t-CNCs on the modulus of polymer nanocomposites containing both CNC species.[22]

The out of plane ductility of the CNC films is tested here in a qualitative fashion (Movies S1–S3, Supporting Information). 3.6 mm wide strips of the films are pinned on one end to a substrate using a strong adhesive (Figure 3f–h). The free end

of the strip is bent slowly toward the pinned end until failure. The maximum angle to horizontal made by the film prior to failure is taken to be a qualitative measure of flexibility. From Figure 3f–h, we find the breaking angle to change from ≈50° in the pristine w-CNC sample to ≈145° in a 5% t-CNC sample. In the 30% sample, however, we observe no failure even up to 180°. The film can be bent to these high angles repeatedly without any perceptible damage. It is noteworthy that even minor enhancements in ductility and modulus such as those seen in the 5% samples result in greatly improved handling ability.

The simultaneous enhancements observed here are highly unusual for manmade systems where increasing strength (or modulus) and toughness are conflicting goals.[1] As discussed earlier, irrespective of the fabrication method (template filling,[46] EISA,[47,48] in situ polymerization[33]), the addition of polymers or plasticizers to helicoidal CNCs results in increased ductility but compromised modulus and strength (Figure 1b). By increasing the polymer content, the materials may gain toughness through intrinsic mechanisms such as molecular uncoiling.[2] However, their ability to tolerate large stresses is sacrificed due to diminished moduli and tensile strengths. In Figure 4a, we plot the properties measured in this study against those measured in literature thus far. The modulus of the periodic region in the mantis shrimp dactyl club,[5] which

**ADVANCED
SCIENCE NEWS**
www.advancedsciencenews.com

**ADVANCED
FUNCTIONAL
MATERIALS**
www.afm-journal.de

Figure 4. a) Comparative Ashby plot of elastic modulus (GPa) versus the strain at break (%) from helicoidal CNC films and composites reported in literature and blended helicoidal CNC films measured here.[25–34] The red line represents the w-CNC ceiling. The black line represents the modulus of the dactyl club periodic region. b) An Ashby plot of elastic modulus (GPa) versus the tensile strength (MPa) comparing the properties of synthetic helicoidal CNC films with those of natural helicoidal materials.

represents an attainable performance goal, is presented as the black line. The maximum achieved pristine helicoidal CNC film modulus, referred to as the w-CNC ceiling, is presented as the red line. From the data, it is clear that the polymer/plasticizer addition moves the chiral films away from the dactyl club values. In contrast, the addition of t-CNC not only moves E and ε_f in the desired direction, it helps photonic films attain properties that rival some of the best natural helicoidal materials, as shown in Figure 4b. The moduli and strength measured here are the highest measured yet in the helicoidal CNC films and their composites.[25–30] The strain to failure and toughness values are some of the best reported for pristine helicoidal CNC films. However, we note that only the data points shown in red (Figure 4a) studied CNC films fabricated using an EISA technique similar to ours. Therefore, we believe that a fair comparison can only be drawn to these data points. Comparing samples with similar strains-to-failure, we find that the t-CNC blends are two to eight times stiffer than w-CNC helicoidal composites that contain as much as 10 to 30% polymer by mass.[25–30] The properties of the 10%, 30%, and 60% t-CNC films are also comparable to those of nacre,[49] one of the strongest and most resilient natural materials known, and that of nacre mimics that have been fabricated using 2D nanoparticles (montmorillonite, graphene oxide).[50,51] However, because the CNC films are lighter (CNC film density ≈1.5 g cm^{-3} (Table S1, Supporting Information), nacre ≈2.45 g cm^{-3}, bone and ivory, ≈1.84 g cm^{-3}, dactyl club >2 g cm^{-3}) they display significantly higher specific stiffness and strength (Figure S5, Supporting Information).
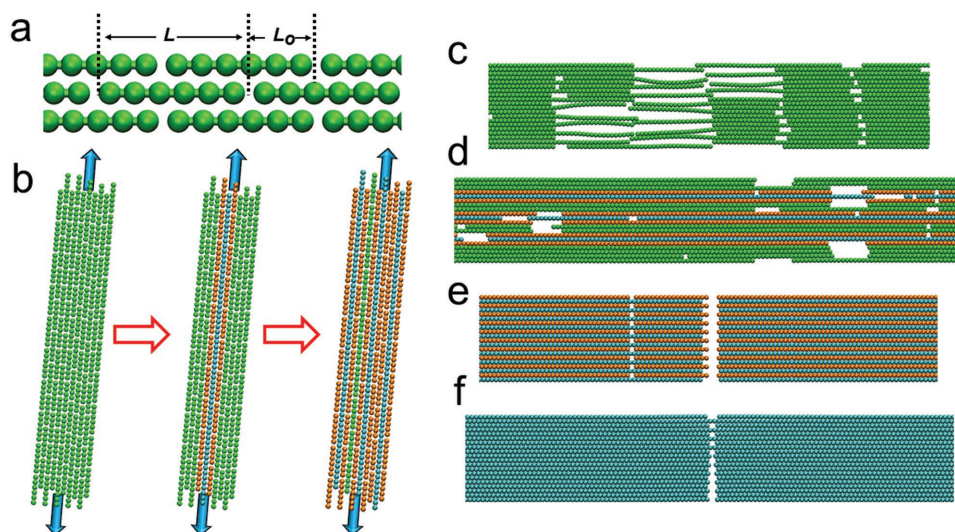
Now we turn our attention toward understanding the cooperative effects on mechanical performance that follow t-CNC addition. While studies report the modulus of individual tunicate nanocrystals to be ≈1.5 times that of individual wood CNCs,[23] linear effective medium approximations fail to model the sigmoidal increase in modulus with t-CNC addition (Figure S6, Supporting Information). More importantly, simply introducing a higher modulus phase does not lead to the concurrent enhancements in strength and ductility seen here.[52] The superior sample crystallinity (χ) with t-CNC introduction ($\chi_{\text{w-CNC}}$ ≈60%, $\chi_{\text{t-CNC}}$ ≈80%[21]) is similarly ineffective

in justifying the observed trends. To better explain the effect of t-CNC addition on the mechanical performance, we carried out molecular dynamics (MD) studies with our atomistically informed coarse-grained (CG) model for CNCs following a strain energy conservation paradigm (**Figure 5**).[39] A simplified cellulose nanocrystal assembly with a layered, staggered, in-plane structure of overlap ratio, $L/L_o = 0.5$ (instead of helicoidal structure) is constructed to represent an individual CNC layer, and subjected to uniaxial tensile tests for structures with different mass fractions of t-CNCs (see the Experiment Section).

When CNC film is strained, the load is initially transferred between the covalent bonds of CNCs through the nonbonded (van der Waals, hydrogen bonds) CNC–CNC interface sites, where the barriers of the sliding energy landscape allow shear transfer.[53] Since the CNCs in each layer of the helicoidal structure are aligned in a staggered fashion as in the layered film structures, the number of nonbonded sites in contact, and thus the magnitude energy barrier to sliding is determined by the overlap length (L_o, Figure 5a) between CNCs. In previous analyses, we have identified enhancements in modulus, strength, and toughness with increasing overlap lengths between CNCs in cellulose nanopaper[39] and graphene sheets in the multi-layered graphene structures, which can be explained through shear-lag type models that capture the length-dependence of the shear strength between high-aspect ratio nanoparticles.[54]

For the pure w-CNC samples, the overlap length is expected to be small (Figure 5a) given the shorter lengths of the crystals. Thus, lower energy barriers to sliding weaken shear transfer and adversely impact modulus and strength. Further, with shorter sliding distances required to pull CNCs apart, the films readily break at low strains (and stresses) (Figure 5c; Movie S4 (0% t-CNC), Supporting Information). When the t-CNCs are introduced into the samples, the effective overlap length of the w-CNCs is improved and the energy barrier for the interfacial sliding (shear transfer efficiency) is greater, resulting in the enhancements in modulus and strength (Figures S6a,b and Movie S5 (20% t-CNC), Supporting Information). We note from the measured dimensions of the two CNC species that each individually dispersed t-CNC may be coordinated with

ADVANCED
SCIENCE NEWS
www.advancedsciencenews.com

ADVANCED
FUNCTIONAL
MATERIALS
www.afm-journal.de

Figure 5. a) Schematic illustrating the overlap length (L_o) parameter in a layer of staggered CNCs. b) Schematic illustrating the effect of t-CNC addition on the overlap length in a layer of CNCs. The green and blue rods represent t-CNCs and w-CNCs, respectively. The orange rods indicate w-CNCs that are coordinated with t-CNCs. As the concentration of t-CNCs increases the average overlap length of w-CNCs increases. The blue arrows indicate the stress-direction relevant to this discussion. Snapshots of the failure mechanisms at different t-CNC mass fractions: c) pure w-CNC nanopaper with strain localization and CNCs pullout failure; d) nanopaper with 15% by mass t-CNCs showing rupture of w-CNCs as a result of increasing effective overlap length, and bridging by t-CNCs and some t-CNC coordinated w-CNCs; e) nanopaper with 50% by mass t-CNCs showing CNCs rupture and saturation in the modulus and strength; and f) pure t-CNC nanopaper with t-CNCs rupture at overlap sites.

up to ≈75 w-CNCs. Evidently, each of these 75 w-CNCs has an overlap length equal to its length ($L ≈ 110$ nm). Since L_o in the neat w-CNC films (≈55 nm) is smaller than L (Figure 5a), the incorporation of t-CNCs is equivalent to increasing the effective overlap length in the samples (Figure 5b), which in turn increases the film modulus and strength (Figure S9, Supporting Information). We note in the 5% and 10% by mass t-CNC samples as many as 25% and 50% of w-CNCs may be coordinated with t-CNCs, assuming perfect dispersion. At these weight fractions (≤30% by mass), the simulations also find the long t-CNCs to serve as rails/bridges that permit the stick-slip translation of w-CNCs, along their length, up to larger strains before pullout, resulting in enhanced ductility, evidenced by larger strains to failure and more pronounced yielding behavior (deviation from linear response) with higher t-CNC content (Figure 3e and Figure 5d). This is akin to the structural role played by the pore canals in crustacean and stomatopods exoskeletons.[55]

Further increasing the effective overlap length, i.e., t-CNC concentration, increases the energy barrier for sliding to values comparable with intra-CNC bond energies, due to which the modulus and strength values plateau. However, beyond a certain critical overlap length the energy barrier to sliding exceeds the strength of CNC, which leads to a gradual transition in the failure mechanism from CNC sliding and pullout to CNC fracture. This is seen here as a loss of ductility in going from the 30% to the 60% and 100% samples (Figures 3 and 5). This lowered strain to failure in the 60% and 100% t-CNC sample is manifested as a reduction in toughness, defined here as the area under the stress–strain curve (Figures 3 and 5f). We find the large overlap length for the pure t-CNC samples leads to large release of energy from CNC–CNC bond rupture with explosive failure (Figure 5e,f). We note that the mechanical

properties from simulations are higher than those from experiments given that the structures used in our simulations are perfectly aligned, while those experimentally measured are helicoidal (Figure S9, Supporting Information). However, when the helicoidal structure is strained in-plane, most of the tensile loads are borne by the layers with CNCs aligned parallel to the tensile direction. Our simplified MD models, representative of these dominant CNC layers, therefore reveal the key structural changes and underlying mechanisms responsible for the observed variations in mechanical properties accompanying the addition of t-CNCs.

The maximum in toughness can also be explained in terms of the maximum elastic strain energy as defined by the shear-lag model developed by Espinosa and co-workers for the brick-and-mortar-like biological composites.[56] These authors noted that beyond a critical overlap length, L_o^* the stiffness saturates, while the shear transfer efficiency between overlapping hard elements drops because a majority of the overlapping region does not carry much shear load. This results in a lowered elastic strain energy density (or toughness) at $L_o > L_o^*$. Using the shear-lag formulation, L_o^* was derived by Espinosa and co-workers to be $≈2.318\sqrt{\dfrac{Ebh}{G}}$.[56] Here, E is the axial elastic modulus of the CNC (105 GPa),[57] G is the shear modulus of CNC–CNC interface, b is half the CNC diameter (3.9 nm ± 0.65 nm), and h is the inter-CNC distance (0.784 nm[53]). Estimating G (≈0.1 GPa) as discussed in the Supporting Information (Figures S6–S8, Supporting Information) and using the known E, b, and h values, L_o^* can be calculated to be ≈131 nm ± 14 nm (the uncertainty is derived from the known variation in b, G, and film modulus). This value is significantly higher than the overlap length achievable using w-CNCs alone

**ADVANCED
SCIENCE NEWS**

www.advancedsciencenews.com

**ADVANCED
FUNCTIONAL
MATERIALS**

www.afm-journal.de

($\approx$55 nm). Thus, to achieve optimal overlap, i.e., to maximize shear transfer efficiency in a w-CNC based system, two broad strategies may be employed: a) The L_o* may be brought down to achievable values by enhancing the CNC–CNC interfacial shear modulus G ($L_o* \propto G^{-0.5}$) or b) the average overlap length in the system may be artificially increased toward L_o* by coordinating w-CNCs with a secondary long-CNC phase (as is done here).

We note that for a well-dispersed system, nearly all w-CNCs are t-CNC coordinated at 30% t-CNC by mass, i.e., $L_{o,30\%} \geq 110$ nm, the average length of a single w-CNC. It is also possible to roughly estimate the L_o at 30% t-CNC, using the shear-lag formulation (see the Supporting Information). At 30% t-CNC, the L_o is found to be 133 ± 20 nm (the uncertainty is derived from known variation in b, G, and E). Remarkably, this value falls near the range of optimal overlap lengths for the w-CNCs studied here. This agreement validates the optimal t-CNC loading identified by our study and additionally, supports the SEM observations that the t-CNCs are indeed well dispersed here. We note that in our simulations, since we use identical cross-sections for both CNC types, the critical overlap length is achieved in a higher mass fraction t-CNC system (Figure S9, Supporting Information). We note that when the t-CNC content is greater than 30% by mass in the binary structures, the percolation of much longer t-CNCs may lead to an increase in the average overlap length to values greater than 110 nm.

The SEM images of fracture cross-sections provide further support to the deformation mechanisms and illuminate additional contributions to toughening by t-CNCs. The pristine w-CNC cross-sections display a clean surface with the characteristic Bouligand patterns (**Figure 6**a), suggesting uninterrupted near-linear crack growth to fracture, i.e., brittle failure. With increasing t-CNC content, we observe a progressive increase in the macro and microscale roughness of the fracture surfaces, a well-established indicator of enhanced toughness in the composite materials (Figure 6a–e; Figure S10, Supporting Information). The increase in surface corrugations (crack tortuosity) at the length scale of the CNCs (Figure S10, Supporting Information) suggests greater extrinsic toughening via crack deflection, extrusion, twisting, and delamination. In all blended samples, the long t-CNCs are also seen bridging microcracks further confirming that they activate additional energy dissipating mechanisms (Figure S11, Supporting Information). Both observations agree with simulation results, which show a similar increase in crack tortuosity and enhanced bridging behavior is with t-CNC addition (Figure 5; Movies S4 and S5, Supporting Information). The fracture surfaces also show several long CNCs that extend several hundred nanometres out from the surface thereby verifying the contribution of the t-CNCs to pullout failure (Figure 6h; Figure S12, Supporting Information). Conceivably, the number of extending t-CNCs increases with increasing mass fraction, suggesting higher
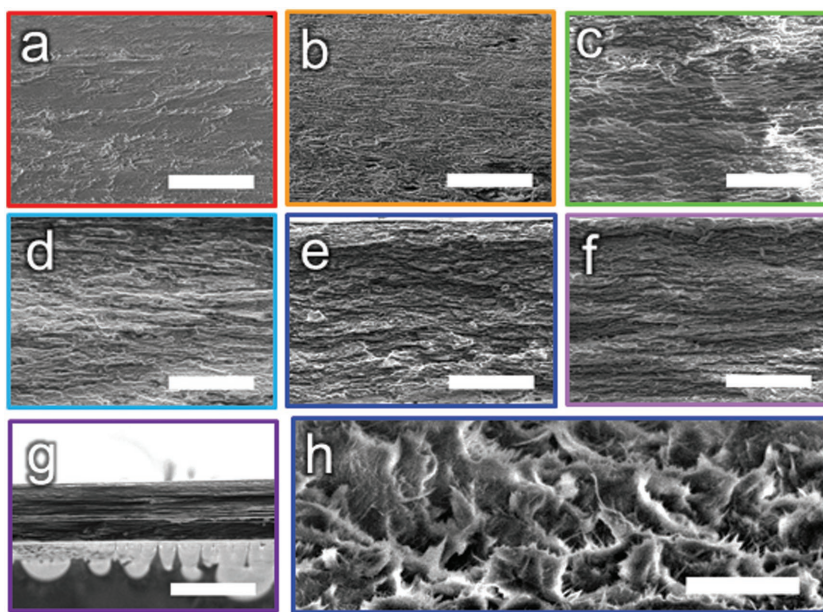
Figure 6. Low-magnification SEM images of the fracture cross sections (stress direction is perpendicular to the page) of a) 0%, b) 1%, c) 5%, d) 10%, e) 30%, f) 60%, and g) 100% by mass t-CNCs, showing increasing macro surface roughness with t-CNC inclusion up to 30% by mass. The scale bars represent 20 µm. h) The SEM image of the fracture cross-section of a mixed w-CNC/t-CNC film with 30% by mass t-CNC, viewed at an oblique angle, showing long t-CNCs extending out the surface. The scale bar represents 4 µm.

contribution to toughness and modulus at higher weight fractions (Figure S12, Supporting Information). While the 60% and 100% t-CNC samples also display pulled-out CNCs, the fracture surfaces are smoother, signifying a more brittle failure through rupture in these samples (Figure 6f,g; Figure S10d, Supporting Information).

3. Conclusion

In conclusion, we have successfully demonstrated a facile strategy to maximize the mechanical performance of the helicoidal CNC films through tailoring the morphology and hierarchical interactions between CNCs. By simply adding a minority population of long t-CNCs to short w-CNCs, we show remarkable improvements in all mechanical performance metrics; a rather unique observation in the realm of the synthetic systems, where properties enhancements are mutually exclusive. These mechanical properties ($E_{30\%}$ = 20.2 GPa ± 0.9 GPa, $\sigma_{f,30\%}$ = 138 MPa ± 4.3 MPa, and toughness$_{30\%}$ = 1.01 MPa m^{-3} ± 0.01 MPa m^{-3}), which are the best reported for the photonic CNC films thus far, rival those of gold-standard natural composites such as cortical bone, nacre, ivory, and stomatopod clubs. It is noteworthy that this study, while providing a strategy to increase overlap lengths in the CNC films, represents the first experimental verification of modeling results that find the overlap length between nanoparticles to strongly influence the properties of their layered ensembles.[39,58] Tunicate nanocrystal addition is also found to control the chiral nematic structure of the dried CNC films. By varying t-CNC concentration, we found films that reflect wavelengths spanning the entire optical

**ADVANCED
SCIENCE NEWS**
www.advancedsciencenews.com

**ADVANCED
FUNCTIONAL
MATERIALS**
www.afm-journal.de

spectrum and the near UV range. By varying the drying rates we expect to extend the range of reflected wavelengths to near-infrared values.[41] While the measured in-plane properties of the CNC films are outstanding, the helicoidal architecture is most advantageous toward out-of-plane properties such as bending modulus, hardness, and impact tolerance.[17,59] Studies to better understand the role of t-CNC inclusion on w-CNC self-assembly, as well as on out-of-plane properties are underway in our lab and will be reported in the due course of time. Meanwhile, we anticipate these sustainably-sourced, light, multifunctional films to find applications in automotive, aerospace, infrastructure, and commercial goods industries in damage tolerant (strong and tough), optically active coatings. Specifically, the UV reflecting properties will enable the use of these materials as UV degradation retarding layers in products exposed to extended periods of sunlight, e.g., solar panels, textiles, etc., and as coatings on electronic displays or eyewear to prevent retinal injury from long-term exposure to blue-UV radiation. More broadly, we expect the results to be adaptable to other CNC types, notably other high-aspect ratio CNCs that are more commercially viable than t-CNCs.

4. Experimental Section

Materials: 11.9% by mass, aqueous suspensions of sodium-neutralized sulphated wood CNCs were obtained from the University of Maine Process Development Center. Tunicate CNCs were obtained by the sulfuric acid hydrolysis of the dry mantles of tunicates (*Styela clava*) using methods described previously.[60]

Sample Preparation: The t-CNCs, as-obtained (0.40% by mass), were found to be aggregated in suspension. The suspensions were diluted to 0.20% by mass and probe sonicated at 30% amplitude for 1 h using 2 s on and off pulses. The sonicated suspension was filtered through 5 µm PTFE filters to retain only the individually dispersed CNCs. Good dispersion of the t-CNCs was verified by studying the permanent birefringence of suspensions and by TEM[60] (Figure S1, Supporting Information). The TEM images of the sonicated t-CNCs were also used to ensure that no significant sonication induced fracturing of the crystals had occurred (Figure 1b). The average length of the t-CNCs was calculated to be (1228 ± 755.5) nm (Figure 1c,d), which was closely matched with measurements of unsonicated t-CNCs made earlier (1330 ± 800) nm.[21]

The filtered t-CNC suspensions and w-CNC suspensions were mixed in desired quantities to reach a total CNC mass fraction of 1.6% and bath sonicated for 1 h. Cholesteric films of varying t-CNC mass fractions (0%, 1%, 5%, 10%, 30%, 60%, 100% by mass) were obtained by evaporation induced self-assembly. The blended CNC water suspensions were cast in a 50 mm diameter polystyrene Petri dish placed inside a sealed Plexiglas chamber at (20 ± 0.5) °C under controlled humidity. The humidity inside the chamber was varied using an evaporation pad with controlled deionized water supply. The mass of the CNC suspension was continuously measured and the relative humidity (RH) inside the chamber was actively corrected to achieve the desired drying rate of −7 mg min⁻¹. When the suspension reached 4.5% by mass of CNCs, the RH was set to 60% to minimize hydration stress and film breakage during drying.

Characterization: The self-assembled architecture of the CNC films was imaged using SEM. Fractured cross-sections of the tensile tested samples and the cross sections of the dried CNC films were coated with a 1 to 2 nm conductive gold–palladium layer. The coated samples were then imaged using an electron beam at a voltage of 5 kV, a current of 50 pA, and a highly-sensitive, high-performance ion conversion and electron secondary electron detector. A working distance of 4 mm was used. TEM was used for the statistical analysis of CNC dimensions. A drop of a dilute CNC suspension was deposited on a carbon-coated TEM grid and dried. The imaging was carried out at 200 kV in bright-field mode. A 40 mm objective aperture and a zero-loss energy filter were inserted to enhance image contrast. No staining was used.

The polarized optical microscopy images of the CNC films with a light absorbing backing (black) surface were obtained using a 5× objective (numerical aperture = 0.13) and a cross polarization setting in reflection mode. It is well known that plane polarized white light incident on the self-assembled CNC films is reflected as circularly polarized light of a wavelength corresponding to the periodicity (pitch) of the helicoidal arrangement. The cross-polarization setting ensures that only this circularly polarized component of the reflected light (i.e., the component Bragg reflected by the chiral CNC structure) is collected. Therefore, the color of the CNC film when imaged in reflection mode using a cross polarizer provides a good estimate of the internal film structure. For a more quantitative estimate, reflectance spectra were recorded at wavelengths spanning 200 nm to 2000 nm (slit widths between 4 and 10 nm) in 1 nm steps using a Perkin Elmer Lambda 950 spectrophotometer equipped with a 150 mm integrating sphere kit. The peak reflectance wavelengths (λ) and the peak widths ($\Delta\lambda$) were measured by fitting the data with single component Gaussian distributions. The in-plane mechanical properties were measured using a RSA G2 Dynamic Mechanical Analyzer, equipped with a 35 N load cell, in constant strain-rate mode. The CNC films were cut into 30 mm × 4 mm strips (and thickness ≈ 50 µm, pure t-CNC sample was 14 µm thick) using low power laser cutting. This ensured that precracks were not introduced during the cutting process, as often observed when using razors or scissors. The gauge length and strain rate used were 22 mm and 0.09 mm min⁻¹, respectively. A sampling rate of 1 second per point was used. All tensile tests were carried out at controlled conditions of (20 ± 1) °C and (45% ± 2%) RH. No conditioning of samples was required. The values reported are averages from testing 5–6 replicates per composite type.

Molecular Dynamics Simulations: CNC nanopaper systems with layered in-plane staggered structure are built as a simplified model to investigate the influence of overlap length on the mechanical performance of the helicoidal structures. The same cross-sections, CG parameters for both t-CNCs and w-CNCs are adopted in our simulations with lowered nonbonded interactions D_0 = 60 kcal mol⁻¹ considering the influence of misalignment of CNCs and other heterogeneities in the helicoidal structures. Each t-CNC consists 360 CG beads (1121.33 nm) and each w-CNC consists 36 beads (112.39 nm), in agreement with experimental observations. The in-plane structures were constructed with 20 rows of CNCs, with each row made with 10 aligned w-CNCs for pure w-CNC samples, and corresponding number of rows (for example, 2 rows with 10% by mass t-CNCs) replaced with t-CNCs considering t-CNC mass fraction. All CG simulations were carried out with large-scale atomic/molecular massively parallel simulator (LAMMPS) and visualizations are done with visual molecular dynamics (VMD).[61,62] The systems with different t-CNC mass fractions (0%, 5%, 10%, 15%, 20%, 30%, 40%, 50%, 100%) were first equilibrated under an NVT ensemble at 300 K for 10 ns followed by an NPT ensemble at 300 K and 0 Pa for another 20 ns with a time step of 10 fs. Then nonequilibrium uniaxial tensile tests along the CNC axial direction are carried out with a constant strain rate of 5 × 10⁻⁹ Å fs⁻¹, and a Berendsen barostat is applied in the other two dimensions to keep the pressure at zero. The mechanical properties were calculated from the stress–strain curves with the same protocols in our former studies, where the stress was calculated from the sum of virial stress over the system and strain is the engineering strain.

Supporting Information

Supporting Information is available from the Wiley Online Library or from the author.

Conflict of Interest

[1] P. Egan, R. Sinko, P. R. LeDuc, S. Keten, *Nat. Commun.* **2015**, *6*, 7418.
[2] C. Zhang, D. A. Mcadams, J. C. Grunlan, *Adv. Mater.* **2016**, *28*, 6292.
[3] S. Nikolov, M. Petrov, L. Lymperakis, M. Friák, C. Sachs, H.-O. Fabritius, D. Raabe, J. Neugebauer, *Adv. Mater.* **2010**, *22*, 519.
[4] H. D. Espinosa, J. E. Rim, F. Barthelat, M. J. Buehler, *Prog. Mater. Sci.* **2009**, *54*, 1059.
[5] J. C. Weaver, G. W. Milliron, A. Miserez, K. Evans-Lutterodt, S. Herrera, I. Gallana, W. J. Mershon, B. Swanson, P. Zavattieri, E. DiMasi, D. Kisailus, *Science* **2012**, *336*, 1275.
[6] M. E. Launey, M. J. Buehler, R. O. Ritchie, *Annu. Rev. Mater. Res.* **2010**, *40*, 25.
[7] D. Raabe, C. Sachs, P. Romano, *Acta Mater.* **2005**, *53*, 4281.
[8] B. Achrai, H. D. Wagner, *Acta Biomater.* **2013**, *9*, 5890.
[9] P. Y. Chen, A. Y. M. Lin, Y. S. Lin, Y. Seki, A. G. Stokes, J. Peyras, E. A. Olevsky, M. A. Meyers, J. McKittrick, *J. Mech. Behav. Biomed. Mater.* **2008**, *1*, 208.
[10] Y. Bouligand, *Tissue Cell* **1972**, *4*, 189.
[11] N. A. Yaraghi, N. Guarín-Zapata, L. K. Grunenfelder, E. Hintsala, S. Bhowmick, J. M. Hiller, M. Betts, E. L. Principe, J.-Y. Jung, L. Sheppard, R. Wuhrer, J. McKittrick, P. D. Zavattieri, D. Kisailus, *Adv. Mater.* **2016**, *28*, 6835.
[12] N. Guarín-Zapata, J. Gomez, N. Yaraghi, D. Kisailus, P. D. Zavattieri, *Acta Biomater.* **2015**, *23*, 11.
[13] Y. Yang, Z. Chen, X. Song, Z. Zhang, J. Zhang, K. K. Shung, Q. Zhou, Y. Chen, *Adv. Mater.* **2017**, *29*, 1605750.
[14] L. J. Bonderer, A. R. Studart, L. J. Gauckler, *Science* **2008**, *319*, 1069.
[15] F. Bouville, E. Maire, S. Meille, B. van de Moortèle, A. J. Stevenson, S. Deville, *Nat. Mater.* **2014**, *13*, 508.
[16] D. Zhao, V. Gimenez-Pinto, A. M. Jimenez, L. Zhao, J. Jestin, S. K. Kumar, B. Kuei, E. D. Gomez, A. S. Prasad, L. S. Schadler, M. M. Khani, B. C. Benicewicz, *ACS Cent. Sci.* **2017**, *3*, 751.
[17] L. K. Grunenfelder, N. Suksangpanya, C. Salinas, G. Milliron, N. Yaraghi, S. Herrera, K. Evans-Lutterodt, S. R. Nutt, P. Zavattieri, D. Kisailus, *Acta Biomater.* **2014**, *10*, 3997.
[18] J. P. F. Lagerwall, C. Schütz, M. Salajkova, J. Noh, J. Hyun Park, G. Scalia, L. Bergström, *NPG Asia Mater.* **2014**, *6*, e80.
[19] I. Usov, G. Nyström, J. Adamcik, S. Handschin, C. Schütz, A. Fall, L. Bergström, R. Mezzenga, *Nat. Commun.* **2015**, *6*, 7564.
[20] R. J. Moon, A. Martini, J. Nairn, J. Simonsen, J. Youngblood, *Chem. Soc. Rev.* **2011**, *40*, 3941.
[21] I. A. Sacui, R. C. Nieuwendaal, D. J. Burnett, S. J. Stranick, M. Jorfi, C. Weder, E. J. Foster, R. T. Olsson, J. W. Gilman, *ACS Appl. Mater. Interfaces* **2014**, *6*, 6127.
[22] J. Sapkota, A. Shirole, E. J. Foster, J. C. Martinez Garcia, M. Lattuada, C. Weder, *Polymer* **2017**, *110*, 284.
[23] Y. Habibi, L. A. Lucia, O. J. Rojas, *Chem. Rev.* **2010**, *110*, 3479.
[24] B. Natarajan, J. W. Gilman, *Philos. Trans. A* **2017**, *376*, 20170050.
[25] B. Wang, A. Walther, *ACS Nano* **2015**, *9*, 10637.
[26] B. Zhu, R. Merindol, A. J. Benitez, B. Wang, A. Walther, *ACS Appl. Mater. Interfaces* **2016**, *8*, 11031.
[27] R. Bardet, N. Belgacem, J. Bras, *ACS Appl. Mater. Interfaces* **2015**, *7*, 4010.
[28] M. Gu, C. Jiang, D. Liu, N. Prempeh, I. I. Smalyukh, *ACS Appl. Mater. Interfaces* **2016**, *8*, 32565.
[29] G. Guidetti, S. Atifi, S. Vignolini, W. Y. Hamad, *Adv. Mater.* **2016**, *28*, 10042.
[30] K. Yao, Q. Meng, V. Bulone, Q. Zhou, *Adv. Mater.* **2017**, *29*, 1701323.
[31] B. Vollick, P.-Y. Kuo, H. Thérien-Aubin, N. Yan, E. Kumacheva, *Chem. Mater.* **2017**, *29*, 789.
[32] P. Liu, X. Guo, F. Nan, Y. Duan, J. Zhang, *ACS Appl. Mater. Interfaces* **2017**, *9*, 3085.
[33] M. Tatsumi, Y. Teramoto, Y. Nishio, *Biomacromolecules* **2012**, *13*, 1584.
[34] J. O. Zoppe, L. Grosset, J. Seppälä, *Cellulose* **2013**, *20*, 2569.
[35] R. Rusli, S. J. Eichhorn, *Appl. Phys. Lett.* **2008**, *93*, 33111.
[36] R. R. Lahiji, X. Xu, R. Reifenberger, A. Raman, A. Rudie, R. J. Moon, *Langmuir* **2010**, *26*, 4480.
[37] T. Saito, R. Kuramae, J. Wohlert, L. A. Berglund, A. Isogai, *Biomacromolecules* **2013**, *14*, 248.
[38] B. Natarajan, N. Lachman, T. Lam, D. Jacobs, C. Long, M. Zhao, B. L. Wardle, R. Sharma, J. A. Liddle, *ACS Nano* **2015**, *9*, 6050.
[39] X. Qin, S. Feng, Z. Meng, S. Keten, *Cellulose* **2017**, *24*, 3289.
[40] S. Mueller, C. Weder, E. J. Foster, *RSC Adv.* **2014**, *4*, 907.
[41] B. Natarajan, C. Emiroglu, J. Obrzut, D. M. Fox, B. Pazmino, J. F. Douglas, J. W. Gilman, *ACS Appl. Mater. Interfaces* **2017**, *9*, 14222.
[42] D. Gubb, *Tissue Cell* **1975**, *7*, 19.
[43] P. G. de Gennes, J. Prost, *Physics Today* **1993**.
[44] J. Pan, W. Hamad, S. K. Straus, *Macromolecules* **2010**, *43*, 3851.
[45] X. M. Dong, T. Kimura, J.-F. Revol, D. G. Gray, *Langmuir* **1996**, *12*, 2076.
[46] S. H. M. Mehr, M. Giese, H. Qi, K. E. Shopsowitz, W. Y. Hamad, M. J. MacLachlan, *Langmuir* **2013**, *29*, 12579.
[47] M. Giese, M. K. Khan, W. Y. Hamad, M. J. MacLachlan, *ACS Macro Lett.* **2013**, *2*, 818.
[48] C. C. Y. Cheung, M. Giese, J. A. Kelly, W. Y. Hamad, M. J. MacLachlan, *ACS Macro Lett.* **2013**, *2*, 1016.
[49] R. O. Ritchie, *Nat. Mater.* **2011**, *10*, 817.

[50] P. Podsiadlo, A. K. Kaushik, E. M. Arruda, A. M. Waas, B. S. Shim, J. Xu, H. Nandivada, B. G. Pumplin, J. Lahann, A. Ramamoorthy, N. A. Kotov, *Science* **2007**, *318*, 80.

[51] J. Wang, J. Qiao, J. Wang, Y. Zhu, L. Jiang, *ACS Appl. Mater. Interfaces* **2015**, *7*, 9281.

[52] A. Dufresne, M. Paillet, J. L. Putaux, R. Canet, F. Carmona, P. Delhaes, S. Cui, *J. Mater. Sci.* **2002**, *37*, 3915.

[53] R. Sinko, S. Keten, *J. Mech. Phys. Solids* **2015**, *78*, 526.

[54] W. Xia, L. Ruiz, N. M. Pugno, S. Keten, *Nanoscale* **2016**, *8*, 6456.

[55] N. A. Yaraghi, N. Guarín-Zapata, L. K. Grunenfelder, E. Hintsala, S. Bhowmick, J. M. Hiller, M. Betts, E. L. Principe, J.-Y. Jung, L. Sheppard, R. Wuhrer, J. McKittrick, P. D. Zavattieri, D. Kisailus, *Adv. Mater.* **2016**, *28*, 6769.

[56] X. Wei, M. Naraghi, H. D. Espinosa, *ACS Nano* **2012**, *6*, 2333.

[57] S. J. Eichhorn, R. J. Young, *Cellulose* **2001**, *8*, 197.

[58] D. D. Hsu, W. Xia, J. Song, S. Keten, *ACS Macro Lett.* **2016**, *5*, 481.

[59] L. K. Grunenfelder, S. Herrera, D. Kisailus, *Small* **2014**, *10*, 3207.

[60] O. van den Berg, J. R. Capadona, C. Weder, *Biomacromolecules* **2007**, *8*, 1353.

[61] W. Humphrey, A. Dalke, K. Schulten, *J. Mol. Graphics* **1996**, *14*, 33.

[62] S. Plimpton, *J. Comput. Phys.* **1995**, *117*, 1.

1800032 (11 of 11)